Multiple Dirac nodal lines in an in-plane anisotropic semimetal $TaNiTe_5$

Zhanyang Hao,[1,*] Weizhao Chen,[1,*] Yuan Wang,[1] Jiayu Li,[1] Xiao-Ming Ma,[1] Yu-Jie Hao,[1] Ruie Lu,[1] Zecheng Shen,[1] Zhicheng Jiang,[2,3] Wanling Liu,[2] Qi Jiang,[2] Yichen Yang,[2] Xiao Lei,[1,4] Le Wang,[1] Ying Fu,[1,5] Liang Zhou,[1] Lianglong Huang,[1] Zhengtai Liu,[2] Mao Ye,[2] Dawei Shen,[2] Jiawei Mei,[1] Hongtao He,[1] Cai Liu,[1] Ke Deng,[1] Chang Liu,[1] Qihang Liu,[1,6,7,†] and Chaoyu Chen[1,‡]

[1]*Shenzhen Institute for Quantum Science and Engineering (SIQSE) and Department of Physics, Southern University of Science and Technology (SUSTech), Shenzhen 518055, People's Republic of China*

[2]*State Key Laboratory of Functional Materials for Informatics and Center for Excellence in Superconducting Electronics, Shanghai Institute of Microsystem and Information Technology, Chinese Academy of Sciences, Shanghai 200050, People's Republic of China*

[3]*Center of Materials Science and Optoelectronics Engineering, University of Chinese Academy of Sciences, Beijing 100049, People's Republic of China*

[4]*Department of Physics, The Hong Kong University of Science and Technology, Clear Water Bay, Hong Kong, People's Republic of China*

[5]*Institute of Applied Physics and Materials Engineering, University of Macau, Avenida da Universidade Taipa, Macau 999078, People's Republic of China*

[6]*Guangdong Provincial Key Laboratory for Computational Science and Material Design, Southern University of Science and Technology, Shenzhen 518055, People's Republic of China*

[7]*Shenzhen Key Laboratory of Advanced Quantum Functional Materials and Devices, Southern University of Science and Technology, Shenzhen 518055, People's Republic of China*

(Received 2 April 2021; revised 10 August 2021; accepted 8 September 2021; published 27 September 2021)

Nodal-line semimetals (NLSMs) contain Dirac-Weyl-type band-crossing nodes extending into shapes of lines, loops, and chains in the reciprocal space, leading to band topology and transport responses. Robust NLSMs against spin-orbit coupling typically occur in three-dimensional and in-plane isotropic materials which have more symmetry operations to protect the line nodes of band crossing, while the possibilities in exfoliatable materials with in-plane anisotropy are rarely discussed. Here, we demonstrate a robust NLSM phase in an exfoliatable in-plane anisotropic nonmagnetic semimetal $TaNiTe_5$. Combining angle-resolved photoemission spectroscopy measurements and first-principles calculations, we reveal multiple Dirac-type nodal lines with fourfold degeneracy in $TaNiTe_5$. Our findings suggest rich physics in structurally anisotropic topological materials and call for further functional exploitation based on them.

DOI: 10.1103/PhysRevB.104.115158

I. INTRODUCTION

Symmetry plays an essential role in topological phases of matter because it determines the way in which different wave functions are forced to have the same energy eigenvalue, i.e., degeneracy. When the valence and conduction bands cross and form distinct point-contact nodes instead of opening a gap, the system turns to a topological semimetal [1]. Following the concept of particle physics, such elementary excitations could be described as Dirac [2–8] and Weyl fermions [9–20], as well as triply degenerate [21–24] and double Dirac fermions [25], etc., manifesting phenomena such as ultrahigh mobility [8] and unusual magnetic transport behaviors [26,27]. In addition, the possible nodal structure in topological semimetals could also extend to shapes of lines, loops, and chains in the reciprocal space, leading to the so-called nodal-line semimetals (NLSMs) [2,28–32]. Typically, NLSMs, especially those robust against spin-orbit coupling (SOC), usually occur in three-dimensional (3D) and in-plane isotropic materials with more symmetry operations (e.g., mirror and nonsymmorphic symmetries) that protect the Dirac band crossing [33–41]. In comparison, the possibility of a robust NLSM phase against SOC in exfoliatable materials with strong in-plane anisotropy has rarely been explored [42–44]. Only very recently, indirect evidence of nonsymmorphic symmetry-protected nodal lines from tunneling spectroscopy was reported based on a two-dimensional (2D) platform, tri-atomic-layer bismuth [45]. Direct evidence of robust NLSMs in 2D exfoliatable materials with in-plane anisotropy is still missing.

Here, we report the realization of robust Dirac nodal lines (DNLs), i.e., nodal lines with fourfold degeneracy, in an exfoliatable, in-plane anisotropic nonmagnetic semimetal $TaNiTe_5$. Combining angle-resolved photoemission spectroscopy (ARPES) and density functional theory (DFT) calculations, we reveal that the interplay between nonsymmorphic symmetry and structural anisotropy results in multiple DNLs robust against SOC, as presented by three key features: (1) fourfold degenerate nodes (Dirac cones) at the boundary (Z point) of the bulk Brillouin zone (BZ); (2)

*These authors contributed equally to this work.
†liuqh@sustech.edu.cn
‡chency@sustech.edu.cn

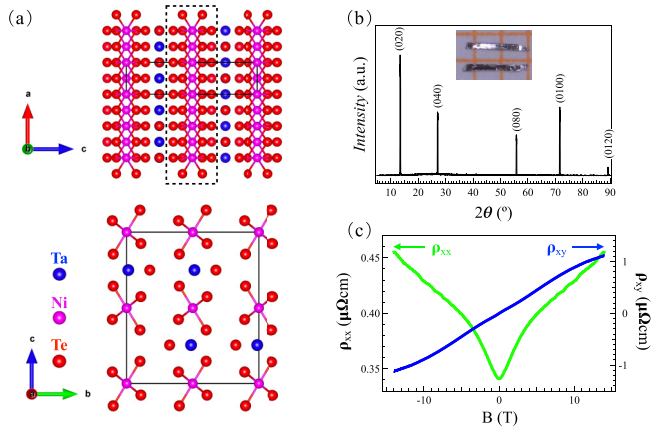

FIG. 1. (a) Schematic lattice structure of $TaNiTe_5$. The single crystals are cleaved along the *ac* plane (top panel) for angle-resolved photoemission spectroscopy (ARPES) measurement. Black solid lines indicate the unit cell, and black dashed box indicates the one-dimensional $NiTe_2$ chains. (b) Single crystal x-ray diffraction (XRD) pattern with all the peaks indexed. The inset shows the optical image of needlelike single crystals. (c) Field-dependent transverse resistivity (ρ_{xx}) and Hall resistivity (ρ_{yx}) measured at 1.6 K for magnetic field parallel to the *b* axis and current parallel to the *a* axis.

these Dirac cones extend through the whole 3D BZ along the *T*-*Z*-*T* line and form DNLs; (3) multiple nodal loops in the *Z*-*A*-*R* plane. The consistency between ARPES measurements and DFT calculations justifies the above claims and provides direct evidence of a NLSM phase robust against SOC in $TaNiTe_5$. Our results suggest rich physics in structurally anisotropic topological materials and call for further functional exploitation based on them.

II. LATTICE STRUCTURE AND CHARACTERIZATION

Single crystals of $TaNiTe_5$ adapt an orthorhombic layered structure with the space group *Cmcm* (No. 63) [46–48]. The lattice constants can be inferred from powder x-ray diffraction (XRD) and single-crystal XRD results with $a = 3.657$ Å, $b = 13.125$ Å, and $c = 15.119$ Å (see the Supplemental Material [49] and Refs. [28,50–57] therein for details). As shown in Fig. 1(a), the one-dimensional (1D) $NiTe_2$ chains extend along the crystallographic *a* axis and form a quasi-2D layer via linking chains of Ta atoms along the *c* axis. For ARPES measurement, cleavage occurs parallel to these *ac* layers ([010]) and normal to the *b* axis. The crystals grow in the shape of needles along the *a* axis [Fig. 1(b) inset]. All the peaks of the single-crystal XRD pattern in Fig. 1(b) can be indexed as (0 *L* 0) reflections, and no trace of an impurity phase can be detected, indicating its high crystalline quality.

Field-dependent resistivity measurement [Fig. 1(c)] was performed with the magnetic field parallel to the *b* axis and current parallel to the *a* axis. The transverse resistivity ρ_{xx} shows linear behavior at low field region (-4 T $< B <$ 4 T), indicating possible linear dispersions close to the Fermi level. No saturation can be inferred for the field up to 15 T. The Hall resistivity shows a generally positive slope with the field and clearly nonlinear behavior, suggesting multiple Fermi surfaces and hole-type carriers. This behavior agrees with recent work

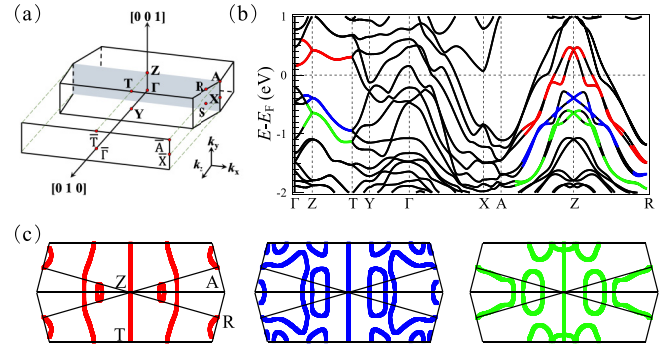

FIG. 2. (a) The three-dimensional (3D) Brillouin zone (BZ) of bulk $TaNiTe_5$ and the projected BZ for the angle-resolved photoemission spectroscopy (ARPES) measured [010] surface with high-symmetry points specified. (b) Density functional theory (DFT) calculated electronic band structure of $TaNiTe_5$ along high-symmetry directions with spin-orbit coupling (SOC), where the three bands with Dirac nodal lines and Dirac cones near the Fermi level are highlighted in red, blue, and green, respectively. (c) The line nodes on the *Z*-*A*-*R* plane for different bands, which correspond to red, blue, and green band crosses as shown in (b).

[46], which reports $TaNiTe_5$ as a material with a nontrivial Berry phase.

III. MULTIPLE DNLs IN $TaNiTe_5$

To uncover the topological properties of $TaNiTe_5$, we start from DFT calculations. Figure 2(b) shows the calculated band structures of $TaNiTe_5$ with SOC on high-symmetry k paths illustrated in Fig. 2(a). Firstly, the band crossings at the *Z* point with linear dispersion in k_x (*Z*-*A*) and k_y (Γ-*Z*) directions, forming the typical fourfold degenerate Dirac cones. This is because nonsymmorphic symmetry $g'_y = \{M_y|(0, \frac{1}{2}, 0)\}$ and $S_{2y} = \{C_{2y}|(0, \frac{1}{2}, 0)\}$ fulfills the anticommutation relationship with inversion at *Z*, leading to an extra twofold degeneracy between two pairs of Kramers doublets. Secondly, along the k_z direction, the Dirac cones extend from point *Z* to point *T*, resulting in robust DNLs against strong SOC. These Dirac cones and DNL features are highlighted in red, blue, and green for the bands near the Fermi level along Γ-*Z*-*T* path shown in Fig. 2(b). Thirdly, the width of the red-labeled band along k_x (*A*-*Z*) direction is ∼2 eV, ∼10 times larger than that along k_y (Γ-*Z*) and k_z (*T*-*Z*), reflecting the anisotropic character of $TaNiTe_5$. In Fig. S2 in the Supplemental Material [49], we perform atomic projection of the DFT calculated dispersion and density of states (DOS). It is shown that, close to the Fermi level, Ta atoms have little contribution to the dispersion and DOS, suggesting that transport electrons are mainly originated from the 1D $NiTe_2$ chains, corroborating its anisotropic nature.

Fourthly, the strongly dispersed bands along the *A*-*Z*-*R* path appear in pairs, forming Type-I Dirac cones on point *Z*, Type-II Dirac cones on point *R*, and cross each other several times forming Type-II Dirac cones in between, which are also highlighted in color in Fig. 2(b). Further DFT calculation confirms that all Dirac cones connect with each other, forming nodal lines and nodal loops on the $k_y = \frac{\pi}{b}$ (*Z*-*A*-*R*) plane, as

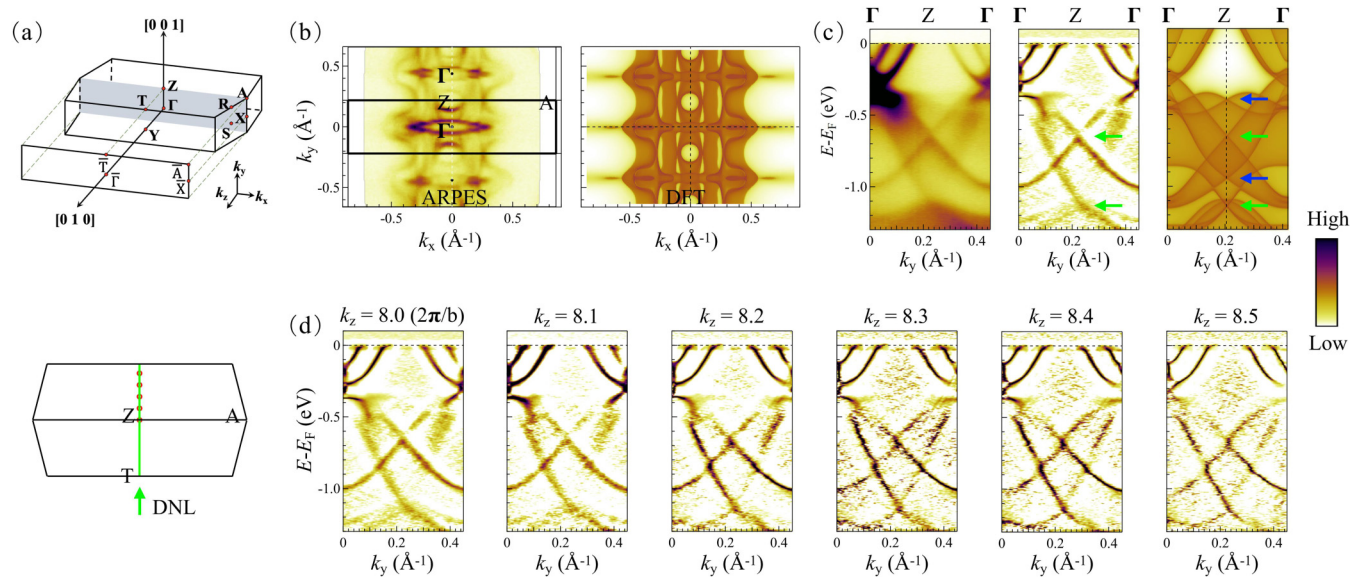

FIG. 3. (a) Schematic three-dimensional (3D) Brillouin zone (BZ) and the location of the Dirac nodal lines (DNLs) along the *T*-*Z*-*T* line in the top *Z*-*A*-*T* plane. Red open circles between *Z* and *T* indicate the positions where angle-resolved photoemission spectroscopy (ARPES) spectra in (d) are taken. (b) Comparison between Fermi surfaces from ARPES (left) and density functional theory (DFT; right) for the single-crystal *ac* plane (Γ-*Z*-*A* plane) of $TaNiTe_5$. (c) Comparison between dispersions along Γ-*Z*-Γ from ARPES raw spectra (left), two-dimensional (2D) curvature (middle), and DFT projection (right). (d) Photon energy-dependent dispersion along $\bar{\Gamma}$-$\bar{T}$-$\bar{\Gamma}$ for k_z covering half of the 3D BZ from *Z* to *T*.

shown in Fig. 2(c). We prove that these DNLs are protected by nonsymmorphic symmetry in the presence of strong SOC in $TaNiTe_5$, establishing a robust NLSM phase (see the Supplemental Material [49] for details).

Our ARPES measurements provide direct evidence of these multiple DNL features. We first analyze the Dirac cone at the bulk *Z* point and DNLs along the *T*-*Z*-*T* line, as indicated in Fig. 3(a). The Fermi surface and bands measured by ARPES and projected from DFT calculations are shown in comparison in Figs. 3(b) and 3(c). For ARPES measurement, the photon energy was selected as 50 eV, so it approximately covers the Γ-*Z*-*A* plane, see Fig. S3 in the Supplemental Material [49] for systematic photon energy-dependent data. Satisfactory agreement between experiment and theory is reached considering the detailed fermiology and spectrum. The fourfold Dirac cone crossing at the bulk *Z* point at −0.64 eV (as discussed in Fig. 2) can be clearly resolved by ARPES, as marked in Fig. 3(c) by green arrows. These measured Dirac cones correspond to the calculated ones shown in green lines in Fig. 2(b). The calculated Dirac cones shown in red lines are above the Fermi level, and those in blue lines are too weak to be resolved [blue arrows in Fig. 3(c)].

Judging from the highlighted dispersion in the curvature plot, this Dirac crossing is gapless at the *Z* point. Furthermore, in Fig. 3(d), we present the spectra of this Dirac crossing at different k_z planes measured by varying the incident photon energies. It is noted that this DNL shows clear dispersion along the *Z*-*T* line in DFT [Fig. 2(b)], with Dirac crossing energy at ∼−0.64 eV at the *Z* point and ∼−1.13 eV at the *T* point. Interestingly, both gapless Dirac crossings are present for all the ARPES spectra at different k_z planes, resulting from the projection of this DNL to the measured k_x-k_y plane, as can be proved by the remarkable agreement between the ARPES spectra and the DFT projection in Fig. 3(c). The manifestation of spectral projection may come from the relatively large Δk_z corresponding with the low photon energies we used. Nevertheless, the photon energy-dependent ARPES measurement corroborates DFT calculations and establishes gapless Dirac cones at bulk *Z*/*T* points and thus a gapless DNL along the *T*-*Z*-*T* line in the 3D BZ, as demanded by $g'_y = \{M_y|(0, \frac{1}{2}, 0)\}$ symmetry (see the Supplemental Material [49] for details).

Considering the nodal loops locating in the *T*-*Z*-*A* plane, we can also find strong evidence of their corresponding Dirac crosses from the satisfactory match between ARPES and DFT. In Fig. 4(a), bottom panel, the nodal loops from three pairs of bands close to the Fermi level are shown in the *T*-*Z*-*A* plane with red, blue, and green colors as in Fig. 2(c). ARPES spectra and DFT dispersion along the k_x ($Z \rightarrow A$) direction are shown in comparison in Figs. 4(b)–4(d). In the present DFT energy-momentum window [Fig. 4(b)], two Dirac crosses can be identified for the green pair of bands, four Dirac crosses for the blue pair, and three for the red, with all the band pairs containing both Type-I and Type-II Dirac cones. The dashed ellipses in Fig. 4(b) point out regions where the Dirac gaps are too small to be resolved in ARPES spectra. Except that, all the features predicted by DFT can be identified in the ARPES spectra, as emphasized in Figs. 4(c) and 4(d) by arrows colored correspondingly. The existence of multiple Type-I and II Dirac crosses along the k_x ($Z \rightarrow A$) direction in ARPES spectra provides strong evidence for the nodal loops shown in Fig. 4(a).

Further evidence of these Dirac crosses can also be derived from the ARPES spectra along the k_y (parallel to Γ-*Z*-Γ) direction at different values of k_x. As shown in Fig. 4(e),

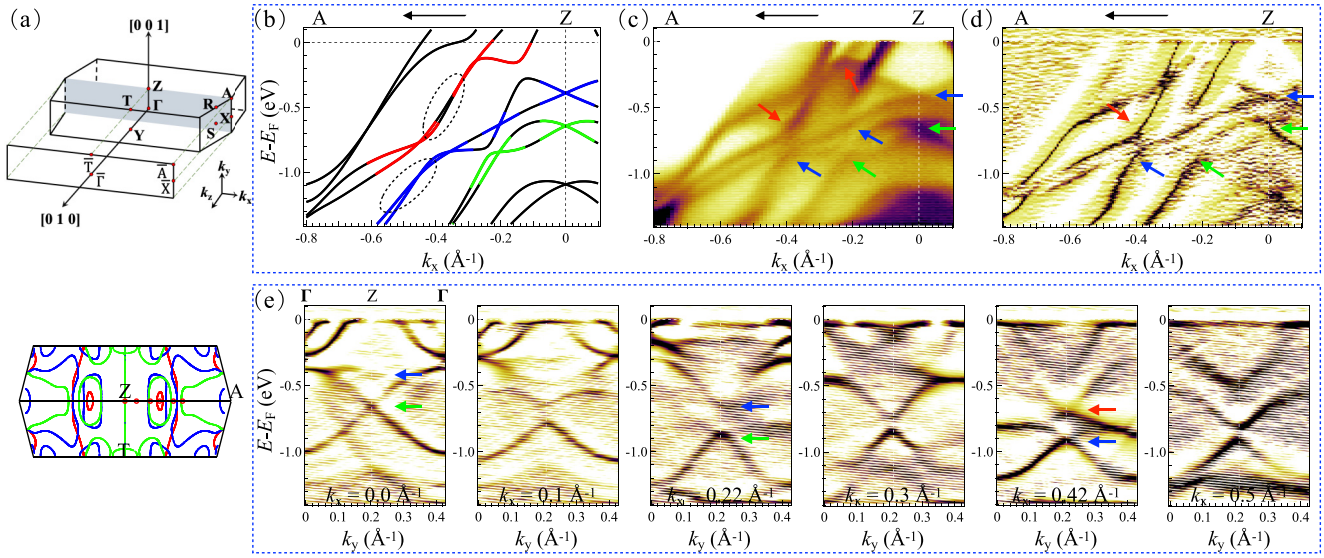

FIG. 4. (a) Schematic three-dimensional (3D) Brillouin zone (BZ) and the location of the nodal loops in the *T*-*Z*-*A* plane. Red solid circles between *Z* and *A* indicate the positions where angle-resolved photoemission spectroscopy (ARPES) spectra in (e) are taken. Comparison between spectra along the $Z \rightarrow A$ direction from (b) density functional theory (DFT) bands, (c) ARPES raw spectra, and (d) two-dimensional (2D) curvature ARPES spectra. (e) Systematic evolution of spectra (2D curvature) along k_y at different k_x values. Colored arrows in (c)–(e) indicate the Dirac crosses from the corresponding band pairs shown in the DFT calculation in (b).

ARPES spectra along the k_y direction at different k_x positions present evolution of the Dirac crosses corresponding to the nodal loop shape. When the k_x positions of the spectra, as specified by red circles in Fig. 4(a), bottom panel, coincide with the nodal loops, gapless Dirac crosses can be identified directly in the 2D curvature spectra. These Dirac crosses are also emphasized by arrows whose colors correspond to the band pairs. When the k_x positions are off the nodal loops, gaps open for the Dirac cone. The correspondence between ARPES and DFT down to a very detailed level establishes solid evidence of multiple Dirac nodal loops in the *T*-*Z*-*A* plane.

IV. SUMMARY

Combining ARPES measurements, DFT calculations, and symmetry analysis, we have demonstrated how structural anisotropy can interact with nonsymmorphic symmetry and reshape the band topology in a semimetal. The resulting multiple robust Dirac crosses and DNLs against SOC suggest fertile physics in lower-dimensional topological systems [58–60]. Compared with their in-plane isotropic counterparts, anisotropic topological materials could be better suited for device exploitation due to their reduced dimensionality, especially in devices utilizing coherent spin transport [61,62]. This paper may stimulate further effort in exploring these rich physics and applications in in-plane isotropic topological materials.

ACKNOWLEDGMENTS

We thank Dr. Peipei Wang and Prof. Liyuan Zhang for assistance in transport measurement. This paper is supported by the National Key R&D Program of China (Grant No. 2020YFA0308900), the National Natural Science Foundation of China (NSFC; Grants No. 12074163 and No. 12074161), NSFC Guangdong (No. 2016A030313650), the Shenzhen High-Level Special Fund (Grants No. G02206304 and No. G02206404), the Guangdong Innovative and Entrepreneurial Research Team Program (Grant No. 2019ZT08C044), the Shenzhen Science and Technology Program (Grant No. KQTD20190929173815000), the University Innovative Team in Guangdong Province (No. 2020KCXTD001), Guangdong Provincial Key Laboratory for Computational Science and Material Design under Grant No. 2019B030301001, the Science, Technology and Innovation Commission of Shenzhen Municipality (No. KQTD20190929173815000), and the Center for Computational Science and Engineering of Southern University of Science and Technology. The authors acknowledge the assistance of SUSTech Core Research Facilities.

[1] N. P. Armitage, E. J. Mele, and A. Vishwanath, Weyl and Dirac semimetals in three-dimensional solids, Rev. Mod. Phys. **90**, 015001 (2018).

[2] A. A. Burkov, M. D. Hook, and L. Balents, Topological nodal semimetals, Phys. Rev. B **84**, 235126 (2011).

[3] Z. Wang, Y. Sun, X.-Q. Chen, C. Franchini, G. Xu, H. Weng, X. Dai, and Z. Fang, Dirac semimetal and topological phase transitions in A_3Bi (A = Na, K, Rb), Phys. Rev. B **85**, 195320 (2012).

[4] S. M. Young, S. Zaheer, J. C. Y. Teo, C. L. Kane, E. J. Mele, and A. M. Rappe, Dirac Semimetal in Three Dimensions, Phys. Rev. Lett. **108**, 140405 (2012).

[5] Z. J. Wang, H. M. Weng, Q. S. Wu, X. Dai, and Z. Fang, Three-dimensional Dirac semimetal and

quantum transport in Cd_3As_2, Phys. Rev. B **88**, 125427 (2013).

[6] Z. K. Liu, J. Jiang, B. Zhou, Z. J. Wang, Y. Zhang, H. M. Weng, D. Prabhakaran, S. K. Mo, H. Peng, P. Dudin, T. Kim, M. Hoesch, Z. Fang, X. Dai, Z. X. Shen, D. L. Feng, Z. Hussain, and Y. L. Chen, A stable three-dimensional topological Dirac semimetal Cd_3As_2, Nat. Mater. **13**, 677 (2014).

[7] Z. K. Liu, B. Zhou, Y. Zhang, Z. J. Wang, H. M. Weng, D. Prabhakaran, S. K. Mo, Z. X. Shen, Z. Fang, X. Dai, Z. Hussain, and Y. L. Chen, Discovery of a three-dimensional topological Dirac semimetal, Na_3Bi, Science **343**, 864 (2014).

[8] M. Neupane, S. Y. Xu, R. Sankar, N. Alidoust, G. Bian, C. Liu, I. Belopolski, T. R. Chang, H. T. Jeng, H. Lin, A. Bansil, F. Chou, and M. Z. Hasan, Observation of a three-dimensional topological Dirac semimetal phase in high-mobility Cd_3As_2, Nat. Commun. **5**, 3786 (2014).

[9] A. A. Burkov and L. Balents, Weyl Semimetal in a Topological Insulator Multilayer, Phys. Rev. Lett. **107**, 127205 (2011).

[10] X. G. Wan, A. M. Turner, A. Vishwanath, and S. Y. Savrasov, Topological semimetal and Fermi-arc surface states in the electronic structure of pyrochlore iridates, Phys. Rev. B **83**, 205101 (2011).

[11] G. Xu, H. Weng, Z. Wang, X. Dai, and Z. Fang, Chern Semimetal and the Quantized Anomalous Hall Effect in $HgCr_2Se_4$, Phys. Rev. Lett. **107**, 186806 (2011).

[12] S. M. Huang, S. Y. Xu, I. Belopolski, C. C. Lee, G. Chang, B. Wang, N. Alidoust, G. Bian, M. Neupane, C. Zhang, S. Jia, A. Bansil, H. Lin, and M. Z. Hasan, A Weyl fermion semimetal with surface Fermi arcs in the transition metal monopnictide TaAs class, Nat. Commun. **6**, 7373 (2015).

[13] A. A. Soluyanov, D. Gresch, Z. Wang, Q. Wu, M. Troyer, X. Dai, and B. A. Bernevig, Type-II Weyl semimetals, Nature (London) **527**, 495 (2015).

[14] H. Weng, C. Fang, Z. Fang, B. Andrei Bernevig, and X. Dai, Weyl Semimetal Phase in Noncentrosymmetric Transition-Metal Monophosphides, Phys. Rev. X **5**, 011029 (2015).

[15] B. Q. Lv, N. Xu, H. M. Weng, J. Z. Ma, P. Richard, X. C. Huang, L. X. Zhao, G. F. Chen, C. E. Matt, F. Bisti, V. N. Strocov, J. Mesot, Z. Fang, X. Dai, T. Qian, M. Shi, and H. Ding, Observation of Weyl nodes in TaAs, Nat. Phys. **11**, 724 (2015).

[16] S.-Y. Xu *et al.*, Discovery of a Weyl fermion state with Fermi arcs in niobium arsenide, Nat. Phys. **11**, 748 (2015).

[17] S.-Y. Xu *et al.*, Discovery of a Weyl fermion semimetal and topological Fermi arcs, Science **349**, 613 (2015).

[18] S.-Y. Xu, C. Liu, S. K. Kushwaha, R. Sankar, J. W. Krizan, I. Belopolski, M. Neupane, G. Bian, N. Alidoust, T.-R. Chang, H.-T. Jeng, C.-Y. Huang, W.-F. Tsai, H. Lin, P. P. Shibayev, F.-C. Chou, R. J. Cava, and M. Zahid Hasan, Observation of Fermi arc surface states in a topological metal, Science **347**, 294 (2015).

[19] L. X. Yang, Z. K. Liu, Y. Sun, H. Peng, H. F. Yang, T. Zhang, B. Zhou, Y. Zhang, Y. F. Guo, M. Rahn, D. Prabhakaran, Z. Hussain, S. K. Mo, C. Felser, B. Yan, and Y. L. Chen, Weyl semimetal phase in the non-centrosymmetric compound TaAs, Nat. Phys. **11**, 728 (2015).

[20] Z. K. Liu, L. X. Yang, Y. Sun, T. Zhang, H. Peng, H. F. Yang, C. Chen, Y. Zhang, Y. F. Guo, D. Prabhakaran, M. Schmidt, Z. Hussain, S. K. Mo, C. Felser, B. Yan, and Y. L. Chen, Evolution of the Fermi surface of Weyl semimetals in the transition metal pnictide family, Nat. Mater. **15**, 27 (2016).

[21] B. Q. Lv, Z. L. Feng, Q. N. Xu, X. Gao, J. Z. Ma, L. Y. Kong, P. Richard, Y. B. Huang, V. N. Strocov, C. Fang, H. M. Weng, Y. G. Shi, T. Qian, and H. Ding, Observation of three-component fermions in the topological semimetal molybdenum phosphide, Nature (London) **546**, 627 (2017).

[22] J. Z. Ma *et al.*, Three-component fermions with surface Fermi arcs in tungsten carbide, Nat. Phys. **14**, 349 (2018).

[23] H. Weng, C. Fang, Z. Fang, and X. Dai, Topological semimetals with triply degenerate nodal points in θ-phase tantalum nitride, Phys. Rev. B **93**, 241202(R) (2016).

[24] Z. Zhu, G. W. Winkler, Q.-S. Wu, J. Li, and A. A. Soluyanov, Triple Point Topological Metals, Phys. Rev. X **6**, 031003 (2016).

[25] B. J. Wieder, Y. Kim, A. M. Rappe, and C. L. Kane, Double Dirac Semimetals in Three Dimensions, Phys. Rev. Lett. **116**, 186402 (2016).

[26] M. Koshino and T. Ando, Anomalous orbital magnetism in Dirac-electron systems: Role of pseudospin paramagnetism, Phys. Rev. B **81**, 195431 (2010).

[27] W. Zhang, R. Yu, W. Feng, Y. Yao, H. Weng, X. Dai, and Z. Fang, Topological Aspect and Quantum Magnetoresistance of β-Ag_2Te, Phys. Rev. Lett. **106**, 156808 (2011).

[28] C. Fang, Y. Chen, H.-Y. Kee, and L. Fu, Topological nodal line semimetals with and without spin-orbital coupling, Phys. Rev. B **92**, 081201(R) (2015).

[29] T. Bzdusek, Q. Wu, A. Ruegg, M. Sigrist, and A. A. Soluyanov, Nodal-chain metals, Nature (London) **538**, 75 (2016).

[30] C. Fang, H. Weng, X. Dai, and Z. Fang, Topological nodal line semimetals, Chin. Phys. B **25**, 117106 (2016).

[31] R. Yu, Z. Fang, X. Dai, and H. Weng, Topological nodal line semimetals predicted from first-principles calculations, Front. Phys. **12**, 127202 (2017).

[32] S.-Y. Yang, H. Yang, E. Derunova, S. S. P. Parkin, B. Yan, and M. N. Ali, Symmetry demanded topological nodal-line materials, Adv. Phys.: X **3**, 1414631 (2018).

[33] J. Hu, Z. Tang, J. Liu, X. Liu, Y. Zhu, D. Graf, K. Myhro, S. Tran, C. N. Lau, J. Wei, and Z. Mao, Evidence of Topological Nodal-Line Fermions in ZrSiSe and ZrSiTe, Phys. Rev. Lett. **117**, 016602 (2016).

[34] L. M. Schoop, M. N. Ali, C. Strasser, A. Topp, A. Varykhalov, D. Marchenko, V. Duppel, S. S. Parkin, B. V. Lotsch, and C. R. Ast, Dirac cone protected by non-symmorphic symmetry and three-dimensional Dirac line node in ZrSiS, Nat. Commun. **7**, 11696 (2016).

[35] B. B. Fu, C. J. Yi, T. T. Zhang, M. Caputo, J. Z. Ma, X. Gao, B. Q. Lv, L. Y. Kong, Y. B. Huang, P. Richard, M. Shi, V. N. Strocov, C. Fang, H. M. Weng, Y. G. Shi, T. Qian, and H. Ding, Dirac nodal surfaces and nodal lines in ZrSiS, Sci. Adv. **5**, eaau6459 (2019).

[36] L. Muechler, A. Topp, R. Queiroz, M. Krivenkov, A. Varykhalov, J. Cano, C. R. Ast, and L. M. Schoop, Modular Arithmetic with Nodal Lines: Drumhead Surface States in ZrSiTe, Phys. Rev. X **10**, 011026 (2020).

[37] Y. Wang *et al.*, Spectroscopic evidence for the realization of a genuine topological nodal-line semimetal in LaSbTe, Phys. Rev. B **103**, 125131 (2021).

[38] Q. Xu, Z. Song, S. Nie, H. Weng, Z. Fang, and X. Dai, Two-dimensional oxide topological insulator with iron-pnictide superconductor LiFeAs structure, Phys. Rev. B **92**, 205310 (2015).

[39] Y. Sun, Y. Zhang, C.-X. Liu, C. Felser, and B. Yan, Dirac nodal lines and induced spin Hall effect in metallic rutile oxides, Phys. Rev. B **95**, 235104 (2017).

[40] J. N. Nelson, J. P. Ruf, Y. Lee, C. Zeledon, J. K. Kawasaki, S. Moser, C. Jozwiak, E. Rotenberg, A. Bostwick, D. G. Schlom, K. M. Shen, and L. Moreschini, Dirac nodal lines protected against spin-orbit interaction in IrO_2, Phys. Rev. Mater. **3**, 064205 (2019).

[41] X. Xu, J. Jiang, W. J. Shi, V. Süß, C. Shekhar, S. C. Sun, Y. J. Chen, S.-K. Mo, C. Felser, B. H. Yan, H. F. Yang, Z. K. Liu, Y. Sun, L. X. Yang, and Y. L. Chen, Strong spin-orbit coupling and Dirac nodal lines in the three-dimensional electronic structure of metallic rutile IrO_2, Phys. Rev. B **99**, 195106 (2019).

[42] S. M. Young and C. L. Kane, Dirac Semimetals in Two Dimensions, Phys. Rev. Lett. **115**, 126803 (2015).

[43] M. Ashton, J. Paul, S. B. Sinnott, and R. G. Hennig, Topology-Scaling Identification of Layered Solids and Stable Exfoliated 2D Materials, Phys. Rev. Lett. **118**, 106101 (2017).

[44] D. Wang, F. Tang, J. Ji, W. Zhang, A. Vishwanath, H. Chun Po, and X. Wan, Two-dimensional topological materials discovery by symmetry-indicator method, Phys. Rev. B **100**, 195108 (2019).

[45] X. Cui, Y. Li, D. Guo, P. Guo, C. Lou, G. Mei, C. Lin, S. Tan, Z. Liu, K. Liu, Z. Lu, H. Petek, L. Cao, W. Ji, and M. Feng, Two-dimensional Dirac nodal-line semimetal against strong spin-orbit coupling in real materials, arXiv:2012.15220.

[46] C. Xu, Y. Liu, P. Cai, B. Li, W. Jiao, Y. Li, J. Zhang, W. Zhou, B. Qian, X. Jiang, Z. Shi, R. Sankar, J. Zhang, F. Yang, Z. Zhu, P. Biswas, D. Qian, X. Ke, and X. Xu, Anisotropic transport and quantum oscillations in the quasi-one-dimensional $TaNiTe_5$: evidence for the nontrivial band topology, J. Phys. Chem. Lett. **11**, 7782 (2020).

[47] Z. Chen, M. Wu, Y. Zhang, J. Zhang, Y. Nie, Y. Qin, Y. Han, C. Xi, S. Ma, X. Kan, J. Zhou, X. Yang, X. Zhu, W. Ning, and M. Tian, Three-dimensional topological semimetal phase in layered $TaNiTe_5$ probed by quantum oscillations, Phys. Rev. B **103**, 035105 (2021).

[48] E. W. Liimatta and J. A. Ibers, Synthesis, structures, and conductivities of the new layered compounds $Ta_3Pd_3Te_{14}$ and $TaNiTe_5$, J. Solid State Chem. **78**, 7 (1989).

[49] See Supplemental Material at http://link.aps.org/supplemental/10.1103/PhysRevB.104.115158 for details of methods, sample characterization, and theoretical analysis.

[50] A. D. Becke, Density-functional thermochemistry. III. The role of exact exchange, J. Chem. Phys. **98**, 5648 (1993).

[51] G. Kresse and J. Furthmüller, Efficient iterative schemes for *ab initio* total-energy calculations using a plane-wave basis set, Phys. Rev. B **54**, 11169 (1996).

[52] G. Kresse and D. Joubert, From ultrasoft pseudopotentials to the projector augmented-wave method, Phys. Rev. B **59**, 1758 (1999).

[53] S. Grimme, Semiempirical GGA-type density functional constructed with a long-range dispersion correction, J. Comput. Chem. **27**, 1787 (2006).

[54] A. A. Mostofi, J. R. Yates, Y.-S. Lee, I. Souza, D. Vanderbilt, and N. Marzari, WANNIER90: A tool for obtaining maximally-localised Wannier functions, Comput. Phys. Commun. **178**, 685 (2008).

[55] N. Marzari, A. A. Mostofi, J. R. Yates, I. Souza, and D. Vanderbilt, Maximally localized Wannier functions: theory and applications, Rev. Mod. Phys. **84**, 1419 (2012).

[56] Q. S. Wu, S. N. Zhang, H.-F. Song, M. Troyer, and A. A. Soluyanov, WANNIERTOOLS: An open-source software package for novel topological materials, Comput. Phys. Commun. **224**, 405 (2018).

[57] P. Tang, Q. Zhou, G. Xu, and S.-C. Zhang, Dirac fermions in an antiferromagnetic semimetal, Nat. Phys. **12**, 1100 (2016).

[58] J. Gooth, B. Bradlyn, S. Honnali, C. Schindler, N. Kumar, J. Noky, Y. Qi, C. Shekhar, Y. Sun, Z. Wang, B. A. Bernevig, and C. Felser, Axionic charge-density wave in the Weyl semimetal $(TaSe_4)_2I$, Nature (London) **575**, 315 (2019).

[59] R. Noguchi *et al.*, A weak topological insulator state in quasi-one-dimensional bismuth iodide, Nature (London) **566**, 518 (2019).

[60] G. Autes, A. Isaeva, L. Moreschini, J. C. Johannsen, A. Pisoni, R. Mori, W. Zhang, T. G. Filatova, A. N. Kuznetsov, L. Forro, W. Van den Broek, Y. Kim, K. S. Kim, A. Lanzara, J. D. Denlinger, E. Rotenberg, A. Bostwick, M. Grioni, and O. V. Yazyev, A novel quasi-one-dimensional topological insulator in bismuth iodide β-Bi_4I_4, Nat. Mater. **15**, 154 (2016).

[61] H.-M. Guo, A brief review on one-dimensional topological insulators and superconductors, Sci. China Phys. Mech. Astron. **59**, 637401 (2016).

[62] D. Kong, J. C. Randel, H. Peng, J. J. Cha, S. Meister, K. Lai, Y. Chen, Z. X. Shen, H. C. Manoharan, and Y. Cui, Topological insulator nanowires and nanoribbons, Nano Lett. **10**, 329 (2010).